Electronic Supplementary Information (ESI) for

Magnesium Fluoride-Engineered UiO-66 Artificial Protection Layers for Dendrite-Free Lithium Metal Batteries

Kunik Jang,‡[a] Hee Jo Song,‡[b] Jung Been Park,[a] Sang Won Jung,[c] and Dong-Wan Kim*[a,c]

[a]School of Civil, Environmental, and Architectural Engineering, Korea University, Seoul 02841, South Korea

[b]Department of Nanotechnology and Advanced Materials Engineering, Sejong University, Seoul 05006, South Korea

[c]KU-LG Energy Solution Department of Battery-Smart Factory, Korea University, Seoul, 02841, South Korea

‡These authors contributed equally to this work.

*Corresponding author

Dong-Wan Kim

E-mail: dwkim1@korea.ac.kr

Experimental section

Materials

Zirconium chloride ($ZrCl_4$) and glacial acetic acid were purchased from Alfa Aesar. Terephthalic acid (H_2BDC), magnesium nitrate hexahydrate ($Mg(NO_3)_2 \cdot 6H_2O$), and ammonium fluoride (NH_4F) were obtained from Sigma-Aldrich. N,N-Dimethylformamide (DMF) and ethanol were purchased from Samchun Chemicals (Korea). Li foil (thickness: 0.75 mm) was purchased from NEBA (Daejeon, Korea). Coin cell assemblies (CR2032-type) and polypropylene separators (PP, Celgard 2400) were prepared by MTI and Wellcos Corporation (Korea), respectively. LiTFSI salt was obtained from Sigma-Aldrich. The 1,3-dioxolane (DOL) and 1,2-dimethoxyethane (DME) electrolytes were purchased from Alfa Aesar.

Preparation of UiO-66 NPs

For the synthesis of UiO-66, 0.96 g of $ZrCl_4$ and 3.6 mL of acetic acid (glacial) were dissolved in 120 mL of DMF to obtain solution A. Simultaneously, 0.72 g of terephthalic acid and 3.6 mL acetic acid (glacial) were also dissolved in 120 mL of DMF to obtain solution B. After stirring each solution for 1 h, solution A was added to solution B under vigorous stirring, followed by stirring for 30 min. The solution was then heated at 120 ℃ using an oil bath for 24 h. Afterward, UiO-66 particles were washed and centrifuged using ethanol more than four times and activated in a vacuum at 150 ℃ for 24 h.

Preparation of I-MgF_2@UiO, C-MgF_2@UiO, F@UiO, and pristine MgF_2

I-MgF_2@UiO was synthesized using as-prepared UiO-66 via a facile solution process. To obtain two solutions, 582.8 mg (2.25 mmol) of $Mg(NO_3)_2 \cdot 6H_2O$ and 170.1 mg (4.5 mmol) of NH_4F were dissolved in 50 mL of deionized (DI) water. Ultrasonic treatment was performed for 30 min to disperse 240 mg of the prepared UiO-66 in a magnesium nitrate hexahydrate

solution. Subsequently, ammonium fluoride solution was slowly added dropwise to the solution containing UiO-66, and the mixture was further stirred for 3 h at room temperature at 300 rpm. A translucent precipitate was collected by centrifugation at 12,000 rpm, washed with ethanol at least four times, and vacuum dried at 150 ℃ for 12 h. The obtained sample was denoted as I-MgF_2@UiO. Additionally, the molar ratio of $NH_4F/Mg(NO_3)_2$ was controlled to 2:2 from 1:2 (I-MgF_2@UiO) to synthesize MgF_2 coated UiO-66 (C-MgF_2@UiO) by adjusting the amount of magnesium nitrate hexahydrate to 1165.6 mg. Pristine MgF_2 was obtained in the absence of the UiO-66 addition step.

Preparation of artificial SEI layer on Li anode

An artificial layer was fabricated on the Li anode in an Ar-filled glove box using the prepared powder. The evenly ground powder and polyvinylidene fluoride (PVDF, Kynar 2801) were homogeneously mixed at a weight ratio of 95:5 with anhydrous DME to form a uniform slurry (0.09 g/ml). Subsequently, 9 μL of the slurry was uniformly dropped onto Li anode (0.95 cm^2) and dried for more than 8 h under vacuum at room temperature.

Characterization

The crystal structure was investigated by XRD (Rigaku, MiniFlex 600 diffractometer) patterns with Cu Kα radiation. Raman spectroscopy (HEDA, WEVE) was used to examine the bonding of MOFs and LiTFSI salts. The electronic structures and composition were investigated by XPS (Nexsa, Thermo Fisher) using Al-Kα radiation. Positive-mode time-of-flight secondary ion mass spectrometry (ToF-SIMS; ION-TOF GmbH, Münster, Germany) was utilized to analyze the composition of the SEI layer. The Bi_3^+ (30 keV) and Cs^+ (10 keV) sputtering guns were used to sputter an area of 50 × 50 and 200 × 200 μm^2. The morphologies of the particles and the deposited Li were verified using field-emission scanning electron

microscopy (FE-SEM; FEI, Quanta FEG 250). The thickness of an artificial layer was observed by focused ion beam and the field emission scanning electron microscope (FIB/SEM; Helios 650, Center for Nanoscale Science and Technology (CNST)). Field-emission transmission electron microscopy (FE-TEM; JEM-F200, JEOL) and EDS were used to analyze the microstructure and elemental distribution. Spherical-aberration-corrected scanning transmission electron microscopy (Cs-STEM; NEO ARM, JEOL) with EDS was used to observe the porous structures. The surface areas and pore volume distributions were estimated using the BET and BJH methods, respectively (BELSORP-max, Microtrac-BEL). The atomic contents were determined by inductively coupled plasma-optical emission spectrometry (ICP-OES; Agilent 5110, Agilent). The static contact angle measurements were performed using a pendant-drop tensiometer (DSA100, KURSS).

Electrochemical measurement

CR2032-type coin cells were used to examine the prepared electrodes. The Li||Li symmetric and LFP||Li full cells were assembled in an Ar-filled glovebox. 60 μL of 1 M LiTFSI in DOL/DME (1:1 vol%) without additives was utilized as the electrolyte for the electrochemical tests. Celgard 2400 was used as the separator for each coin cell. Galvanostatic profiling and CV tests were performed using an automatic battery cycler (4300 K Desktop, MACCOR). EIS was performed using an IVIUM-n-STAT electrochemical analyzer (IVIUM Technologies). The alternating voltage amplitude of the measurements was 10 mV in the frequency range of 100 kHz to 0.01 Hz. To analyze the CE of Li plating/stripping for the asymmetric Li||Cu cell, an artificial layer was coated on Cu foil. CE tests were conducted at a current density of 1 mA cm^{-2}, with a fixed plating capacity of 1 mAh cm^{-2}, and stripping was continued until the voltage reached the cutoff voltage of 0.5 V. The doctor blade casting method was used to fabricate LFP (Johnson Mathey (JM) Co., Ltd.) cathodes for full-cell tests. LFP,

Super P carbon black (Alfa Aesar), and polyvinylidene fluoride (PVDF, Kynar 2801) were blended at (weight ratio of 70:20:10) in N-methylpyrrolidinone (NMP, Sigma-Aldrich) to prepare a homogeneous slurry. The collected slurry was coated on as-prepared Al foil and then dried at 60 ℃ for more than 8 h under vacuum. The mass loading of active material onto each electrode was approximately 1.5 mg cm^{-2}. The rate capability (range 0.5–10 C) and charge/discharge process of the LFP||Li full cell were tested in the voltage window of 2.5–4.2 V.

Computational details

All DFT calculations were implemented using the Quantum Espresso package.[1,2] The exchange-correlation effects were treated within the generalized gradient approximation (GGA) using the Perdew-Burke-Ernzerhof (PBE) functional.[3] The core electrons were described by projector augmented wave (PAW) pseudopotentials. The Grimme DFT-D3 correction method was employed to describe van der Waals (vdW) dispersion interactions.[4] The spin-polarization behavior of the electrons was considered during the calculations. The energy cutoff of 37 Ry was used. A Monkhorst-Pack grid of 2 × 2 × 1 was employed for k-space sampling in MgF_2, and a 1 × 1 × 1 grid was utilized for UiO-66 with F-terminated groups. The convergence criteria for total energy and ionic relaxation loop were set to be less than 10^{-4} eV and 0.03 eV $Å^{-1}$, respectively. A vacuum layer of 15 Å was utilized to inhibit interactions between successive slabs. The binding energy (E_b) was calculated as the following equation:

$$E_b = E_{total} - E_{sub} - E_{ads}$$

where E_{total}, E_{sub}, and E_{ads} refer to the total energies of fully relaxed substates absorbed with DOL, DME and Li, fully relaxed pristine substrates, and adsorbate, respectively.

Ionic conductivity measurement

EIS measurements were conducted on stainless steel (SS)||SS symmetric cells to calculate the ionic conductivities of the artificial SEI layers. Each sample was coated with the same thickness on a SS foil. The ionic conductivity of the symmetric cell was calculated as follows: $\sigma = L/RS$, where σ is ionic conductivity, L is the thickness, R is the bulk resistance obtained from EIS measurement, and S is the area of SS electrode.[5-7]

Li^+ transference number measurement

t_{Li+} was determined by assessing the interfacial resistance before and after potentiostatic polarization and was calculated using the Vincent-Bruce method.[5,6] A polarization voltage (10 mV) was applied for 2000 s until a steady state was reached. Nyquist plots were obtained before and after the polarization process. The t_{Li+} values were calculated based on the following equation: $t_{Li+} = I_{ss}(\Delta V - I_0R_0)/ I_0(\Delta V - I_{ss}R_{ss})$, where I_0 and I_{ss} are initial and steady-state currents, respectively; ΔV is the applied voltage; R_0 and R_{ss} represent the interfacial resistances between the separator and Li anode before and after the polarization.

Activation energy measurement

EIS measurements were performed on Li||Li symmetric cells within the temperature range of 30-50 °C to evaluate the R_{ct}. The activation energy (E_a) was calculated by fitting the temperature-dependent Nyquist plots using the Arrhenius equation:[8,9]

$$\frac{1}{R_{ct}} = A\, exp(\frac{-E_a}{RT})$$

where R_{ct}, A, E_a, R, and T correspond to the charge transfer resistance, frequency factor, activation energy, ideal gas constant, and temperature, respectively.

Supplementary Note 1

To investigate the factors that modify the nanoporous structure of UiO-66, two distinct samples were synthesized by adding $Mg(NO_3)_2$ and NH_4F sources individually. The synthesized samples are denoted as Mg@UiO and F@UiO. As verified by the XRD analysis, Mg@UiO displayed the same distinct phase as UiO-66, whereas F@UiO exhibited an amorphous phase (Fig. S8). This indicated that the transition in the crystal structure was attributed to the introduction of NH_4F. In particular, HF derived from NH_4F aqueous solution can etch the ZrO_x clusters in UiO-66.[10,11] The HF-induced amorphization of UiO-66 was confirmed by etching UiO-66 in an HF solution at the same concentration as that of the NH_4F solution (Fig. S9).

To verify the influence of NH_4F etching on the pore structure, the BJH pore size distribution of F@UiO was analyzed (Fig. S10). F@UiO showed a relatively large average pore size (4.2 nm) and was found to have pore characteristics similar to those observed for I-MgF_2@UiO, indicating that the HF derived from the NH_4F solution etched the ZrO_x clusters in UiO-66, leading to modification of the pore structure (Fig. S7). After MgF_2 permeation to obtain I-MgF_2@UiO, the centrifuged solution was analyzed using ICP-OES to detect the etched ZrO_x clusters. The clear detection of Zr showed that the ZrO_x clusters were partially etched during the reaction, which can elucidate the size deformation of the nanopores by NH_4F etching (Table S1).

Supplementary Note 2

For Mg 1s spectrum of I-MgF_2@UiO, the peaks located at 1305.0 and 1306.4 eV were assigned to Mg-F and $Mg(OH)_{2-x}F_x$ bonds, respectively (Fig. 2a).[12] The high-resolution F 1s spectrum of I-MgF_2@UiO was deconvoluted into two individual peaks consistent with Zr-F (685.0 eV) and Mg-F (686.3 eV), showing a larger Zr-F peak than that of C-MgF_2@UiO (Fig. 2b).[13-15] The observed Zr-F binding implied fluorination of the Zr cluster during NH_4F etching, resulting in the formation of F-terminated groups.[16] For the Zr 3d spectrum of the I-MgF_2@UiO, the fitted peaks appearing at 182.7 (Zr $3d_{5/2}$) and 185.1 eV (Zr $3d_{3/2}$) were matched to Zr-O bonds, while the peaks at 183.6 (Zr $3d_{5/2}$) and 185.8 eV (Zr $3d_{3/2}$) were consistent with Zr-F bonds (Fig. 2c).[14,15,17,18] I-MgF_2@UiO displayed a higher Zr-F/Zr-O ratio than C-MgF_2@UiO, indicating that a larger number of F-terminated groups were formed in I-MgF_2@UiO, which was in good agreement with the Zr 3d spectrum. In the high-resolution O 1s spectrum of I-MgF_2@UiO, the peaks located at 530.2, 531.7, and 534.2 eV were assigned to the Zr-O-Zr (bridging oxygens), Zr-O-C (carboxylate oxygens), and residual $Mg(OH)_{2-x}F_x$ bonds, respectively (Fig. 2d).[19]

Supplementary Note 3

The solvents (DOL/DME), which serve as Lewis bases, bind with Li^+ (Lewis acid), forming a Li^+ solvation sheath through Lewis acid-base interactions.[20-22] To facilitate the desolvation of Li^+, a strong Lewis base (cation receptor) to attract Li^+ or a strong Lewis acid (anion receptor) to attract solvents and anions is required to weaken the interaction between Li^+ and the solvation sheath. The F^- Lewis base sites originating from the F-terminated groups and MgF_2 within I-MgF_2@UiO compete with the solvents.[23] Simultaneously, the Mg^{2+} Lewis acid sites on MgF_2 can strongly adsorb solvents, thereby expediting the desolvation process.[24-26] As verified by the XRD and HRTEM results, the dominant (111) plane of MgF_2 was selected to calculate the binding energies between Li^+ and MgF_2, as well as between the solvents and MgF_2 (Fig. 3d and S13). Moreover, the calculation of the adsorption effect of the F-terminated groups on Li^+ was conducted by substituting one of the BDC (1,4-benzenedicarboxylate) linkers within the UiO-66 framework with the F-terminated groups.

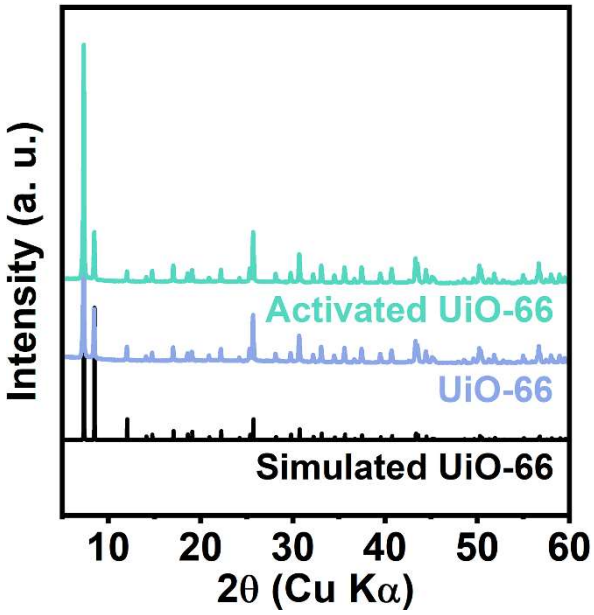

Fig. S1 XRD patterns of activated UiO-66, UiO-66, and simulated UiO-66.

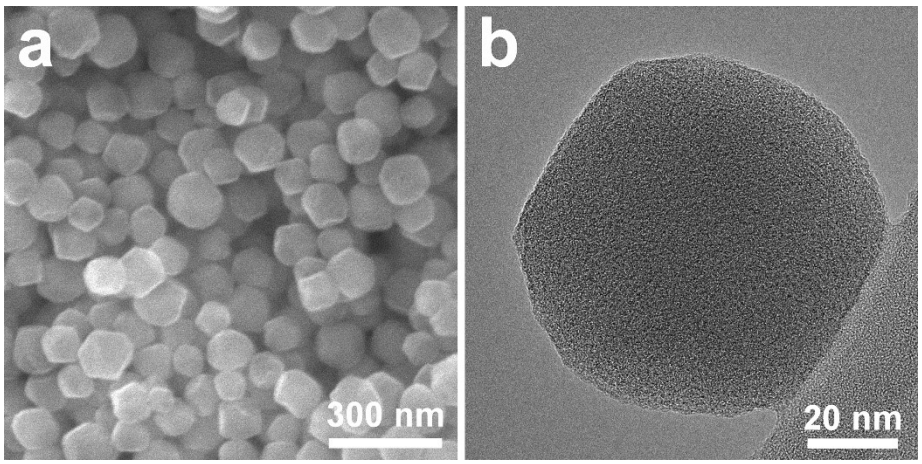

Fig. S2 a) SEM and b) TEM images of UiO-66.

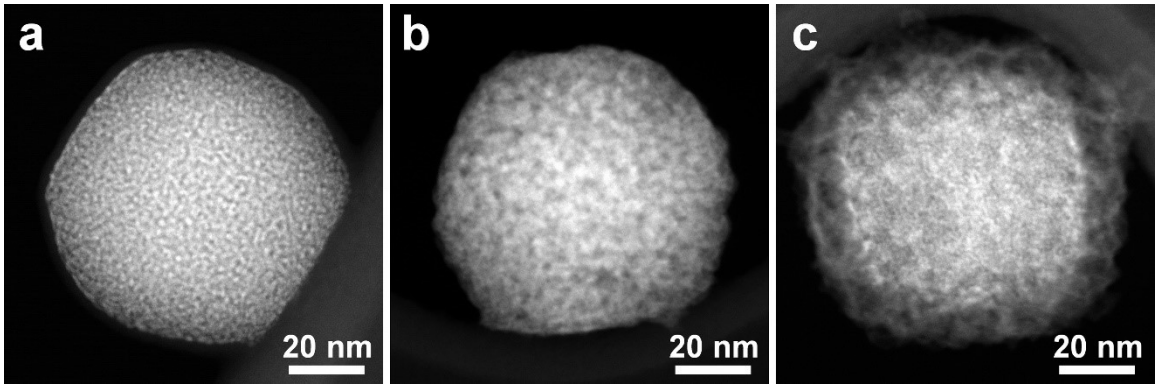

Fig. S3 Dark-field Cs-STEM images of a) UiO-66, b) I-MgF_2@UiO, and c) C-MgF_2@UiO.

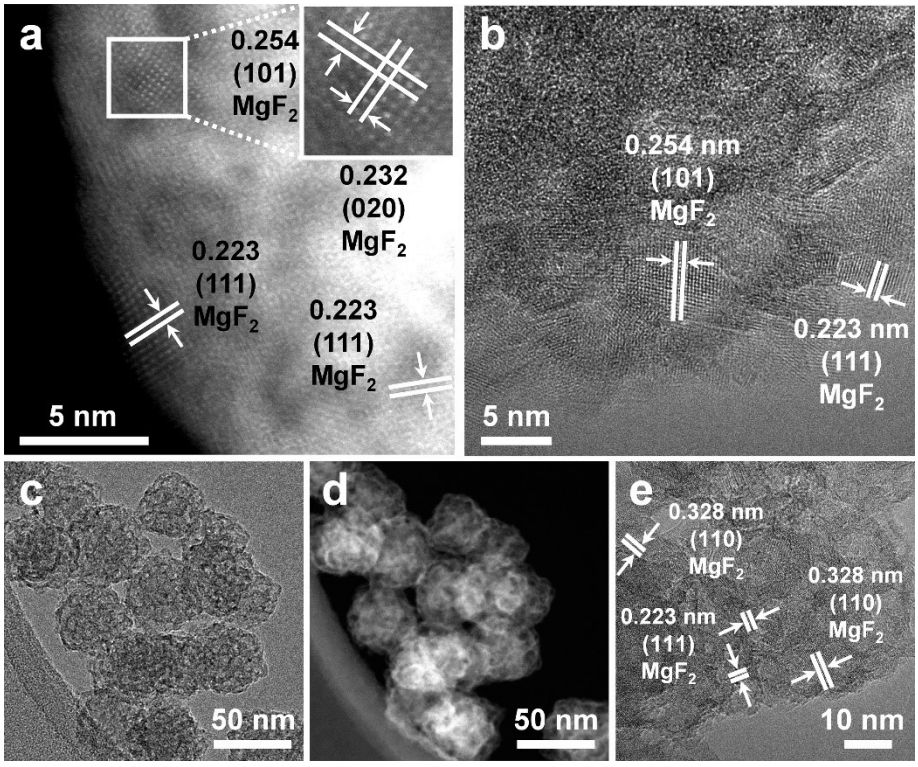

Fig. S4 a) HR-STEM image of I-MgF_2@UiO. HR-TEM images of b) C-MgF_2@UiO and c-e) pristine MgF_2.

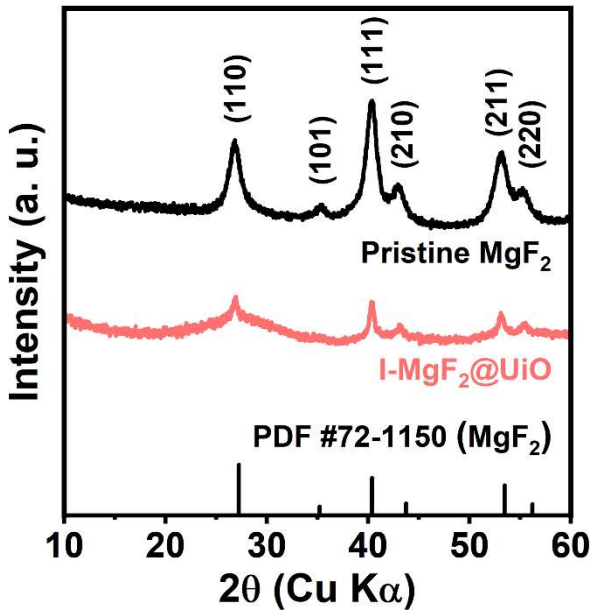

Fig. S5 XRD patterns of pristine MgF_2 and I-MgF_2@UiO.

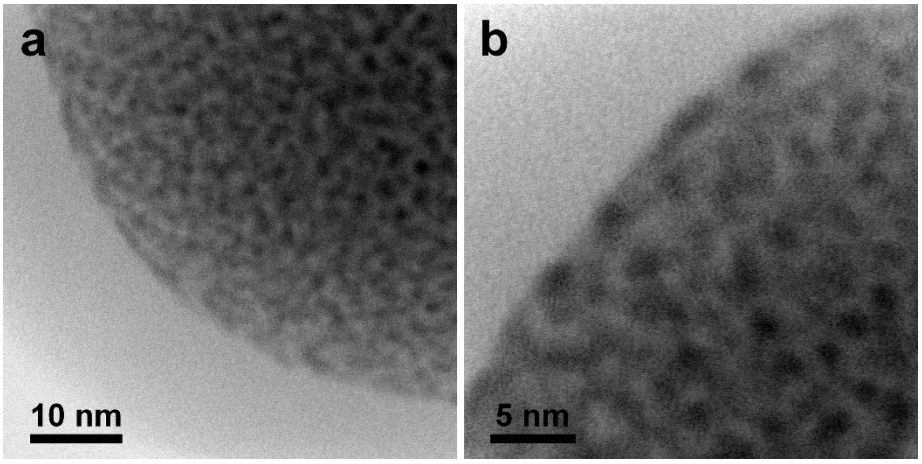

Fig. S6 Bright-field HR-STEM images of UiO-66.

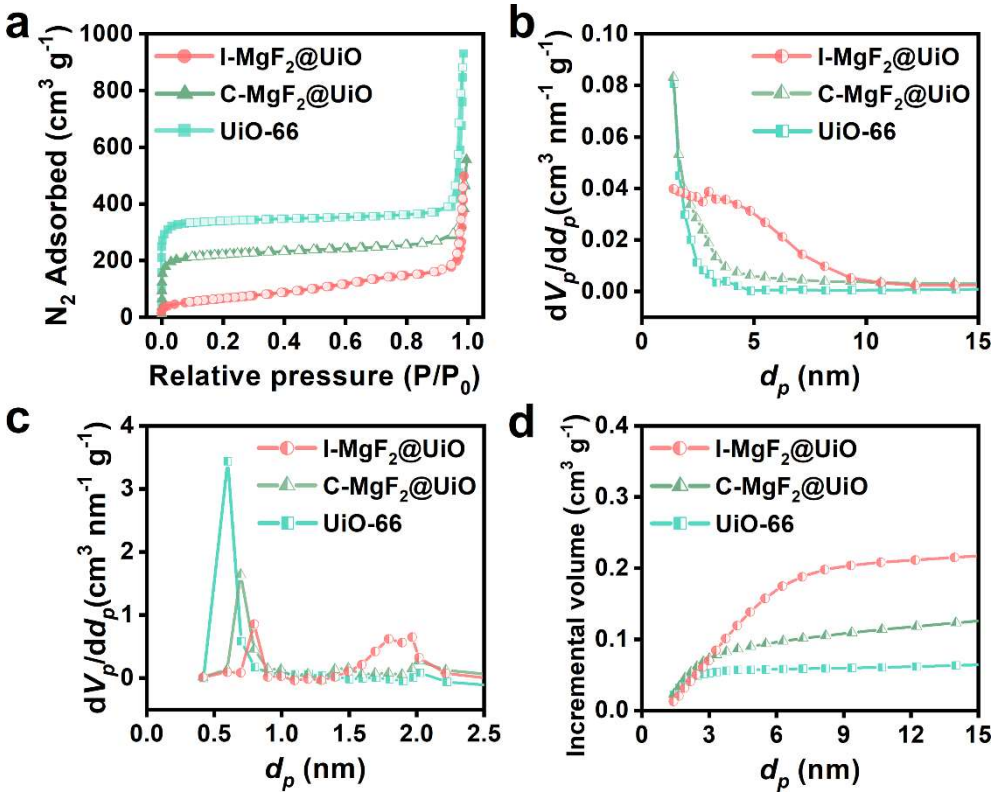

Fig. S7 Plots of a) nitrogen adsorption-desorption isotherms to obtain BET surface areas, b) pore size obtained by BJH, c) micro-pore distribution by MP method, and d) incremental pore volume for I-MgF_2@UiO, C-MgF_2@UiO, and UiO-66.

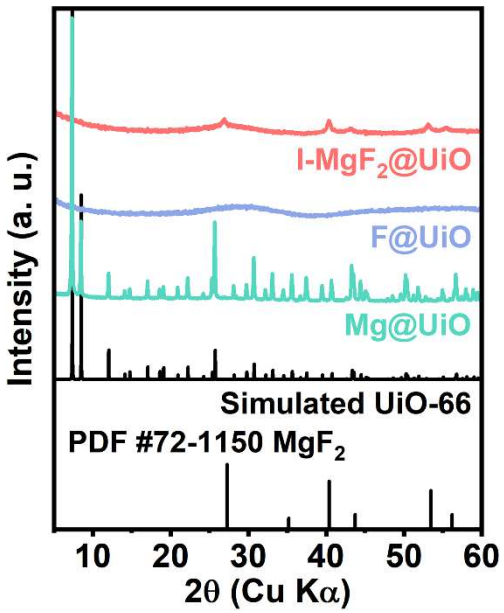

Fig. S8 XRD patterns of Mg@UiO, F@UiO, and simulated UiO-66.

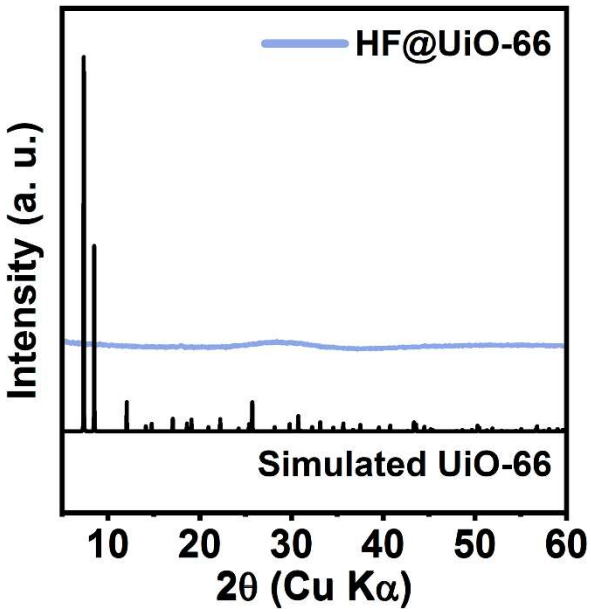

Fig. S9 XRD pattern of UiO-66 etched with diluted HF solution.

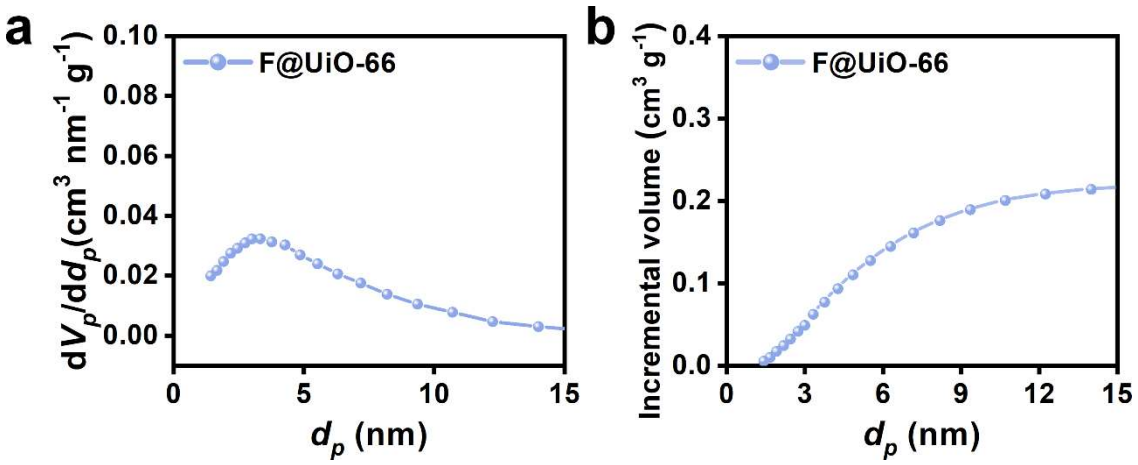

Fig. S10 Plots of a) BJH pore size distribution, and b) incremental pore volume for F@UiO.

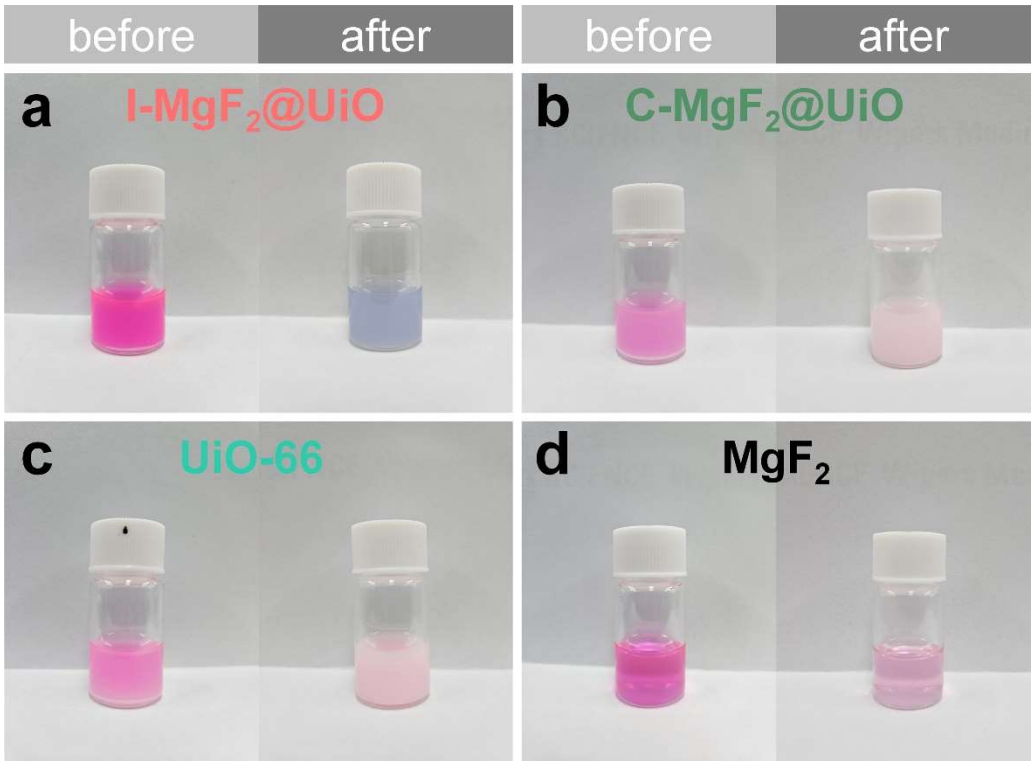

Fig. S11 Photos of rhodamine B dye in dimethylformamide solution containing a) I-MgF_2@UiO, b) C-MgF_2@UiO, c) UiO-66, and d) MgF_2 before (left) and after (right) stirring for 24 h. 20 mg of each powder was immersed in 0.05 mM RhB solution.

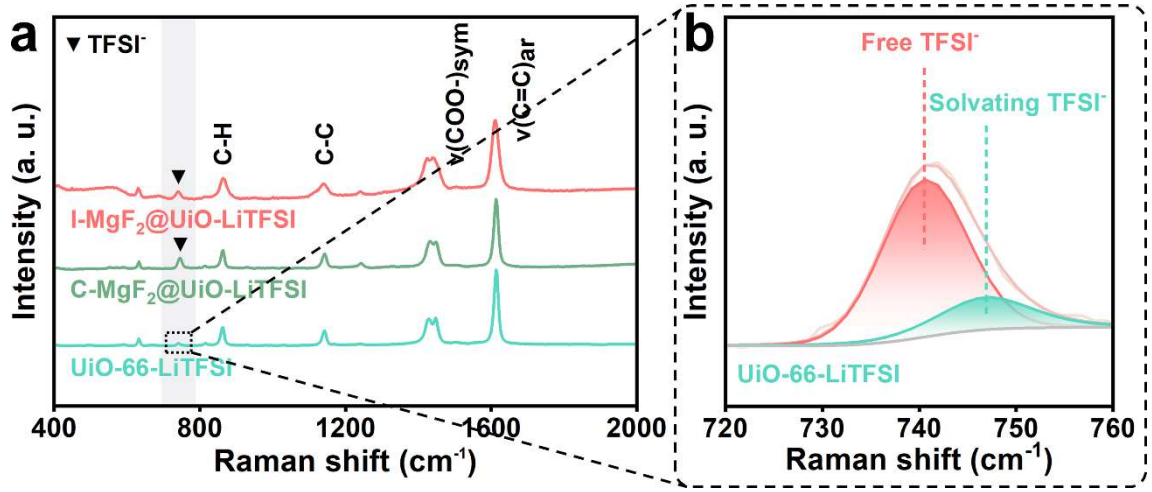

Fig. S12 a) Raman spectra of I-MgF_2@UiO, C-MgF_2@UiO, and UiO-66 after immersion in 1 M LiTFSI in DOL/DME (1:1 vol%) electrolyte for 12 h. b) Magnified Raman spectrum of UiO-66 in the range of 720 to 760 cm^{-1}.

The free $TFSI^-$ band in Fig. S12b indicates that UiO-66 contributes to the dissociation of LiTFSI salts due to its uncoordinated Zr sites.[20] However, the relatively low intensity of the $TFSI^-$ band suggests that UiO-66 plays a minor role in the dissociation of LiTFSI compared to I-MgF_2@UiO. This limited contribution is attributed to the smaller pore size of UiO-66, which impedes the impregnation of LiTFSI (Fig. S7c).[27]

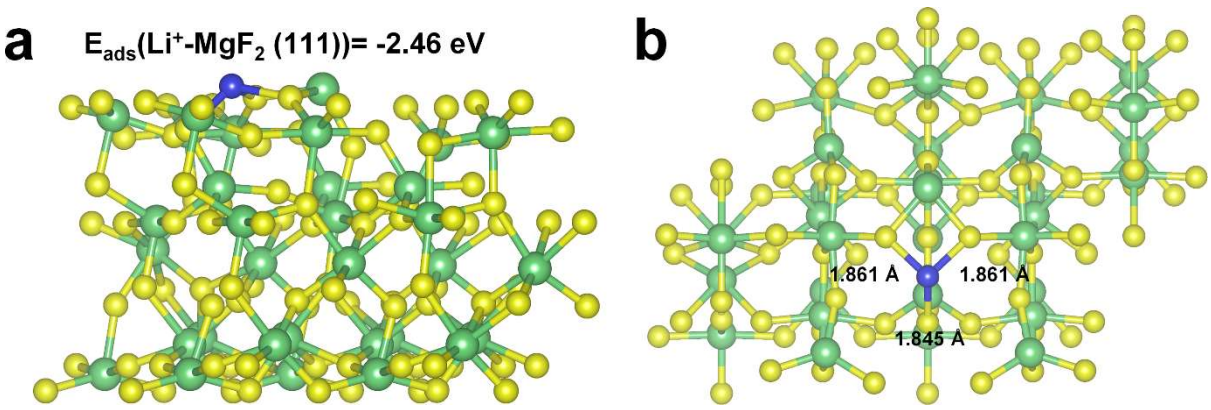

Fig. S13 Adsorption binding energy between Li^+ and MgF_2 (111) plane. a) Side and b) top view of the (111) plane of MgF_2 with Li^+. Li in blue, Mg in light green, and F in yellow.

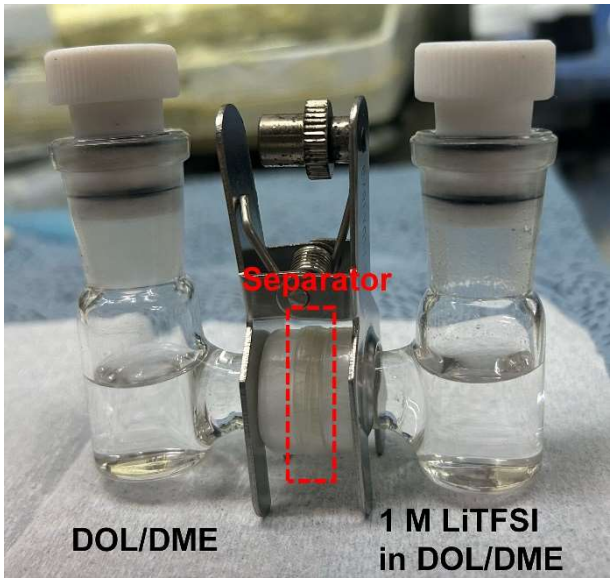

Fig. S14 Photo of H-cell for Li^+ permeability test with 1 M LiTFSI (right side) and DOL/DME (1:1 vol%) (left side).

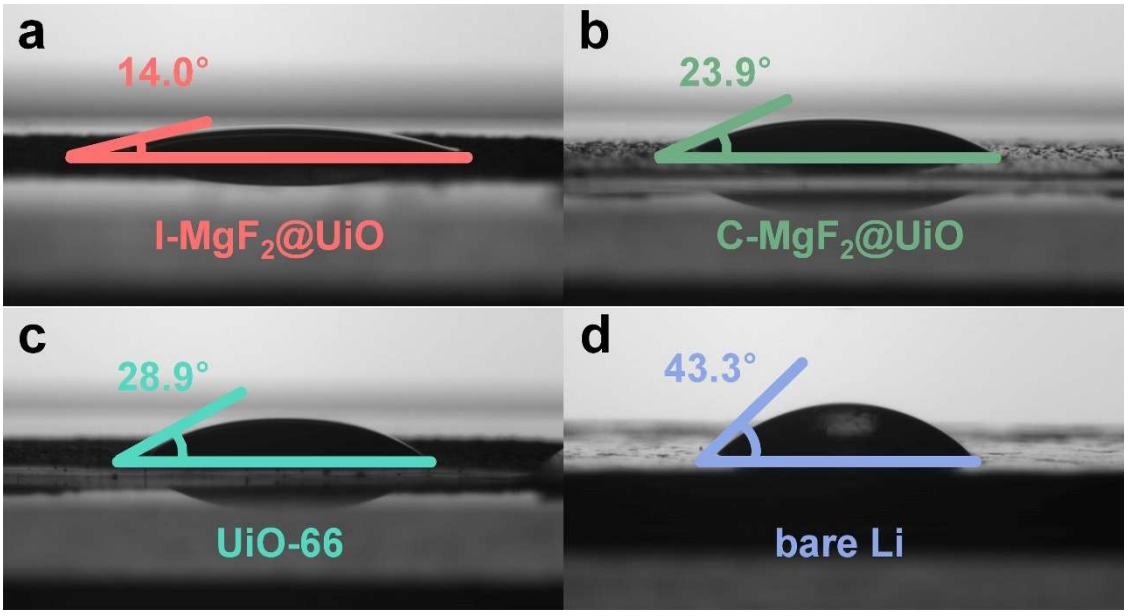

Fig. S15 Contact angles of 1 M LiTFSI in DOL/DME (1:1 vol%) electrolyte on a) I-MgF_2@UiO, b) C-MgF_2@UiO, c) UiO-66, and d) bare Li.

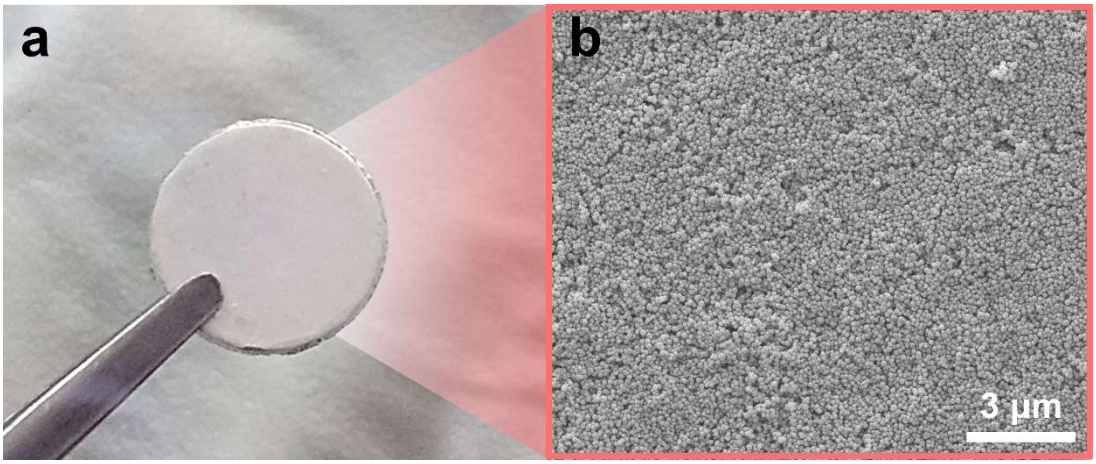

Fig. S16 a) Photo of I-MgF_2@UiO electrode and b) corresponding SEM image.

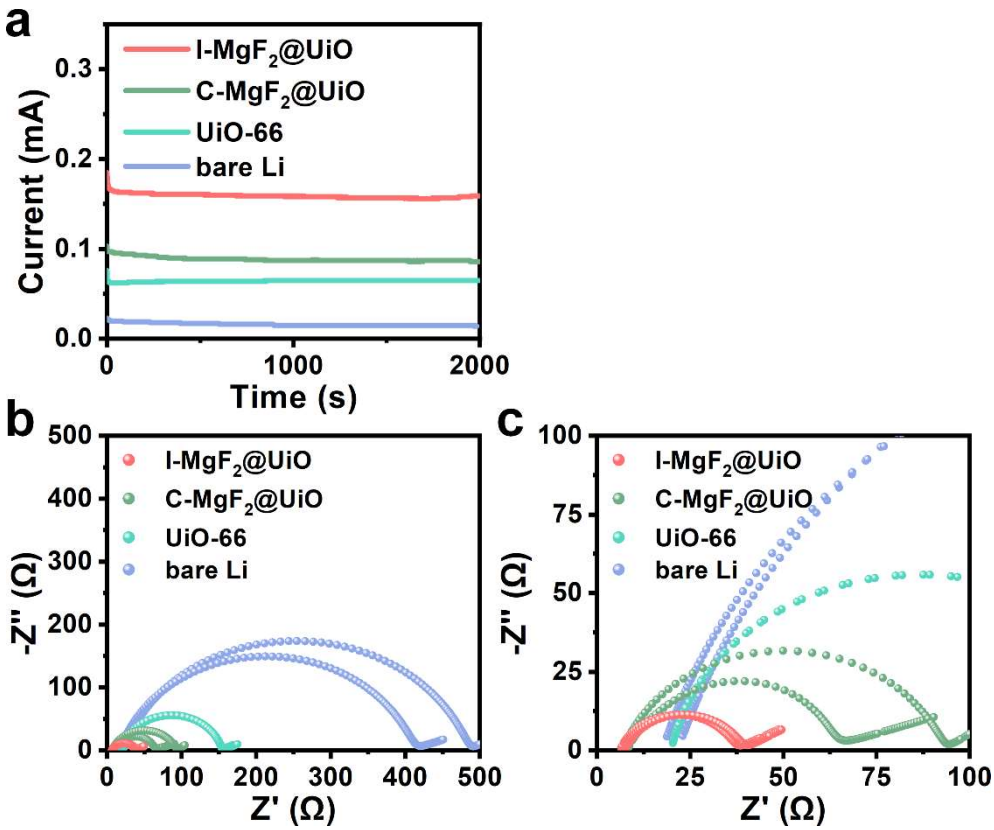

Fig. S17 a) Polarization curves of I-MgF_2@UiO, C-MgF_2@UiO, UiO-66, and bare Li symmetric cells using chronoamperometry measurement at 10 mV. b) Nyquist plots before and after polarization of I-MgF_2@UiO, C-MgF_2@UiO, UiO-66, and bare Li symmetric cells, and c) corresponding magnified high-frequency region.

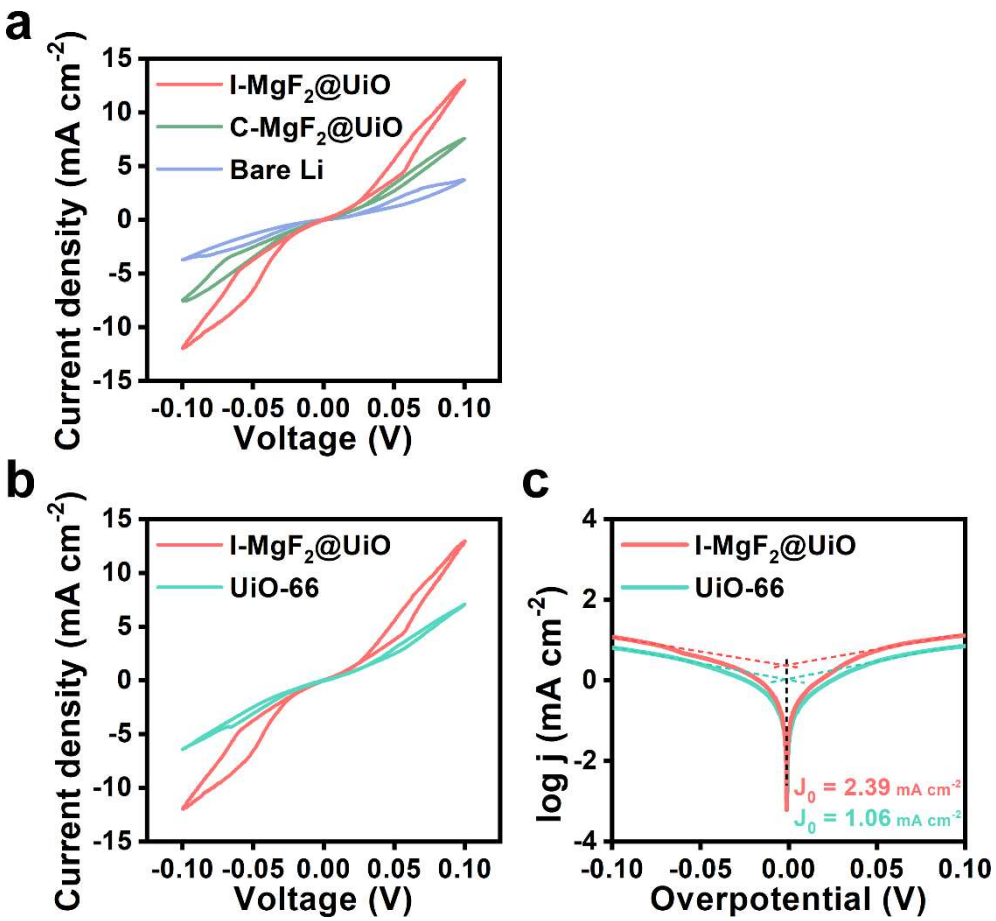

Fig. S18 a) CV curves in the range of -0.1 V to 0.1 V at 0.1 mV s^{-1} of I-MgF_2@UiO, C-MgF_2@UiO, and bare Li symmetric cells. b) CV curves of I-MgF_2@UiO and UiO-66 symmetric cells, and c) corresponding tafel plots to derive the exchange current density.

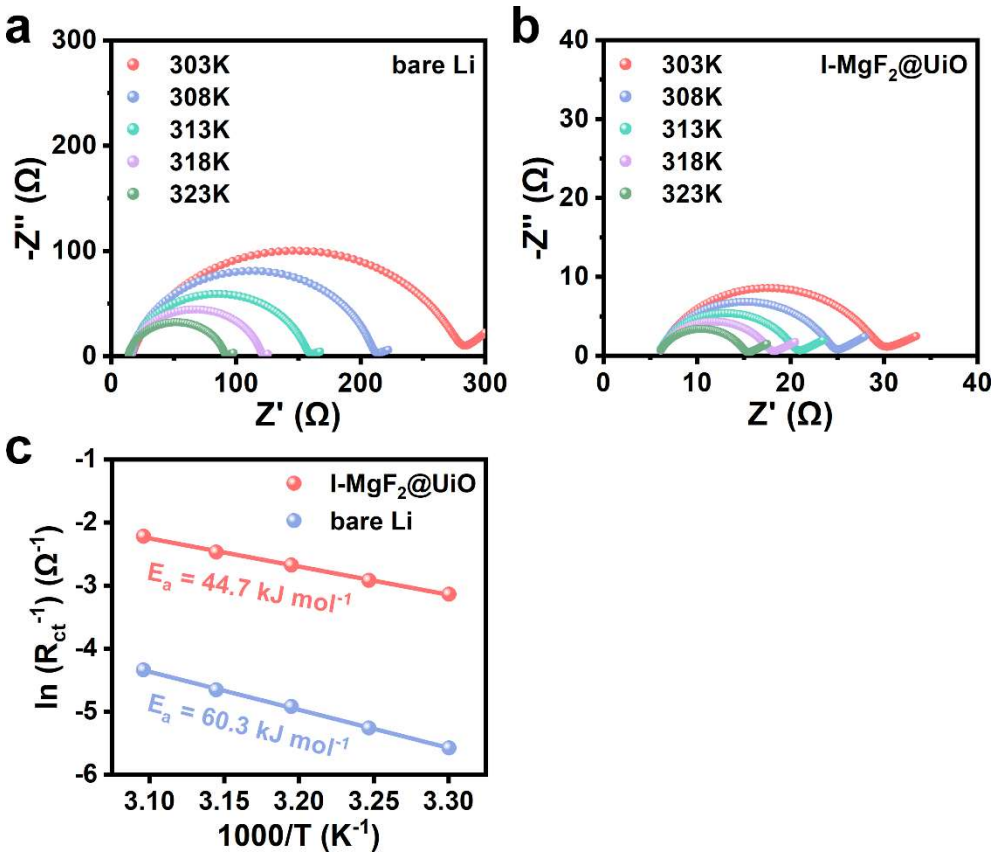

Fig. S19 Nyquist curves of symmetric cells at various temperatures for a) bare Li and b) I-MgF_2@UiO. c) The corresponding Arrhenius curves and calculated activation energies.

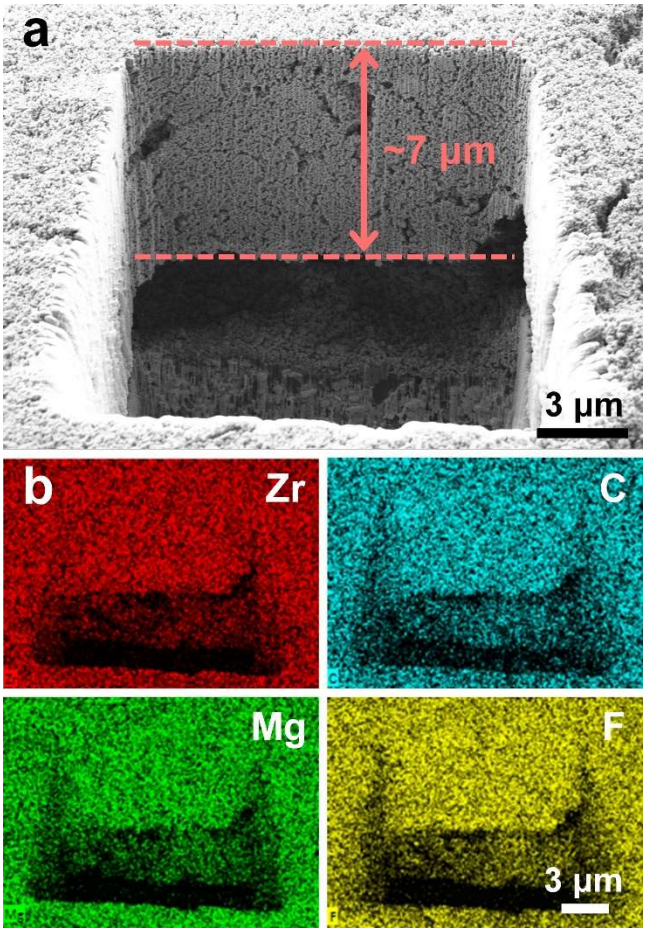

Fig. S20 a) Cross-sectional FIB-SEM image and b) corresponding EDS mapping images of Li deposition on I-MgF_2@UiO electrode with a plating capacity of 3 mAh cm^{-2}.

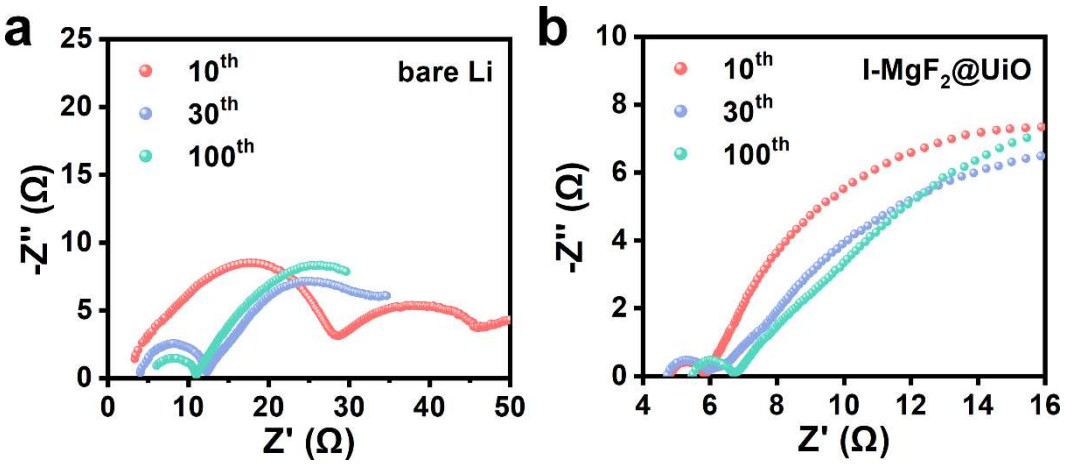

Fig. S21 Nyquist plots of a) bare Li and b) I-MgF_2@UiO symmetric cells after 10^{th}, 30^{th}, and 100^{th} cycles.

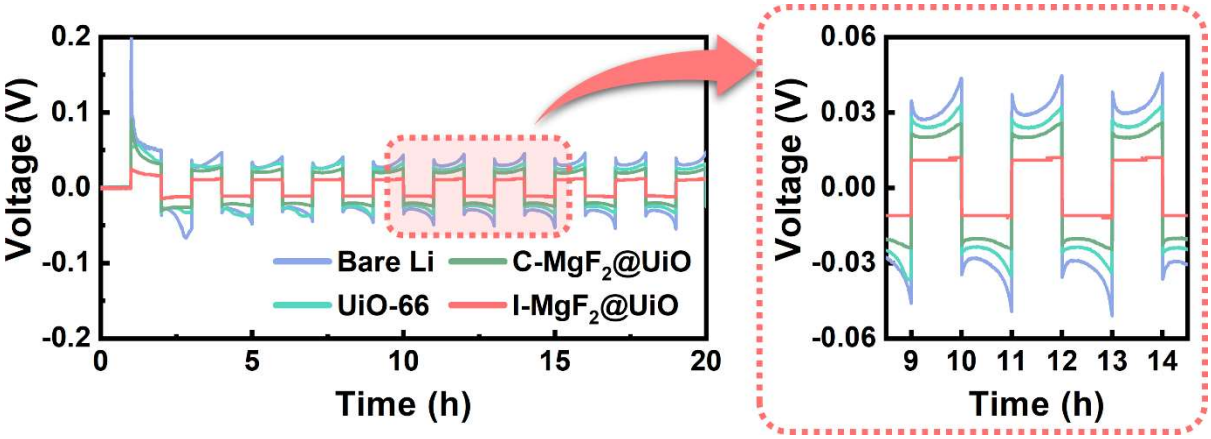

Fig. S22 Magnified section of Figure 5c, showing a range of 0 to 20 h.

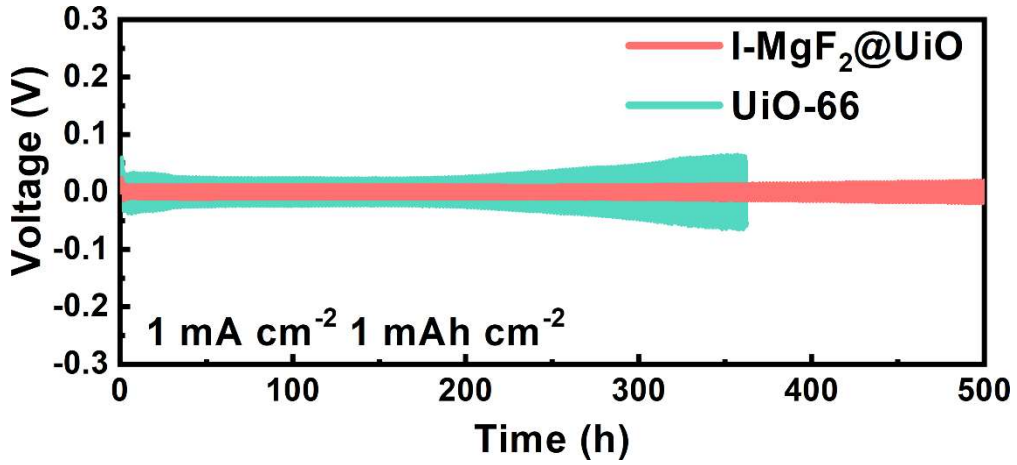

Fig. S23 Voltage profiles of Li||Li symmetric cells with I-MgF_2@UiO, and UiO-66 at 1 mA cm^{-2} and a capacity of 1 mAh cm^{-2}.

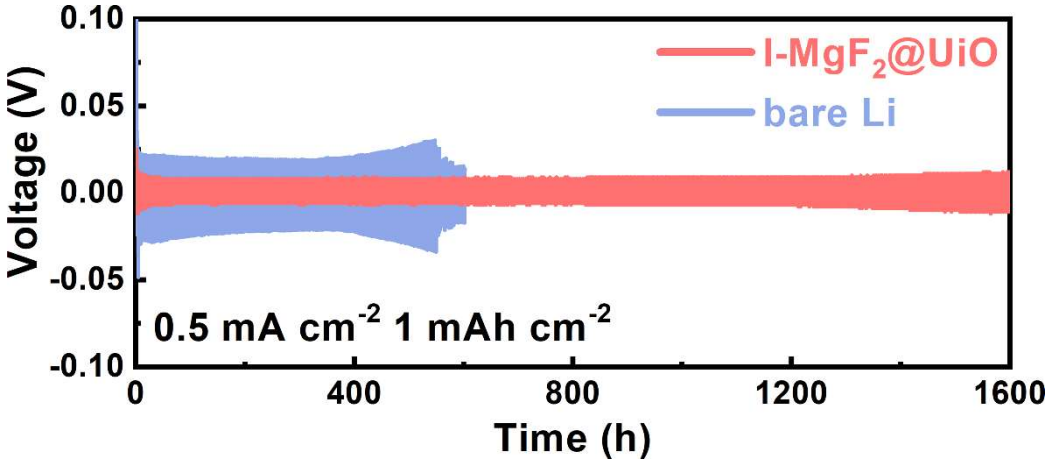

Fig. S24 Voltage profiles of Li||Li symmetric cells with I-MgF_2@UiO, and bare Li at 0.5 mA cm^{-2} and a capacity of 1 mAh cm^{-2}.

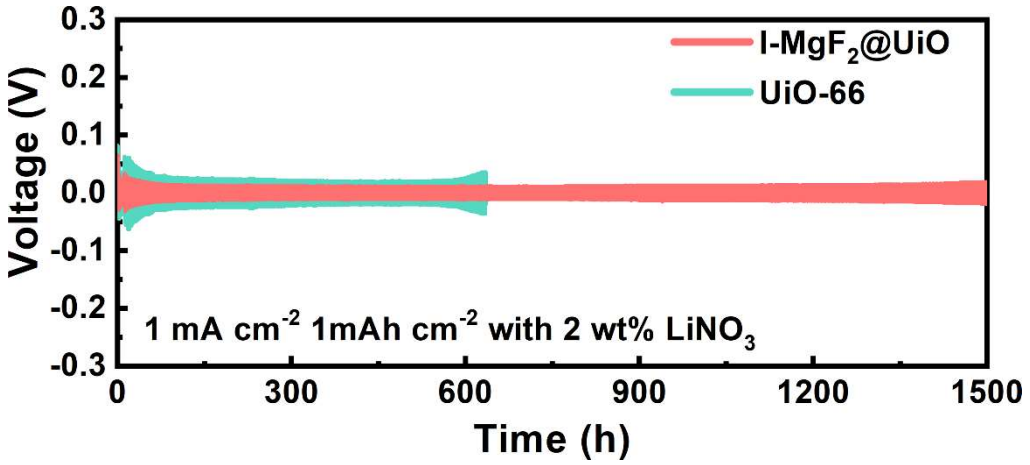

Fig. S25 Voltage profiles of Li||Li symmetric cells with I-MgF_2@UiO, and UiO-66 at 1 mA cm^{-2} and a capacity of 1 mAh cm^{-2} with addition of 2 wt% $LiNO_3$ additive.

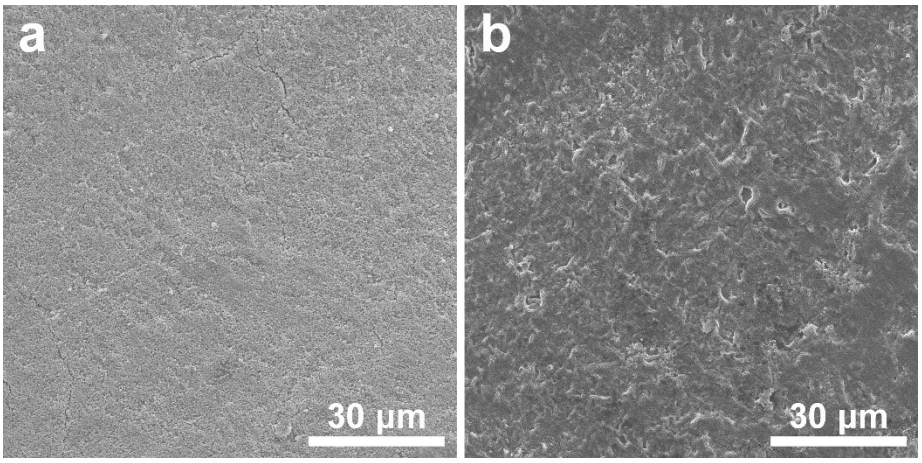

Fig. S26 Ex-situ SEM images of I-MgF_2@UiO electrode a) before and b) after removal of the coating layer, after the 100 cycles of Li plating/stripping at 1 mA cm^{-2} and a capacity of 1 mAh cm^{-2} using 1 M LiTFSI in DOL/DME (1:1 vol%) without any additives.

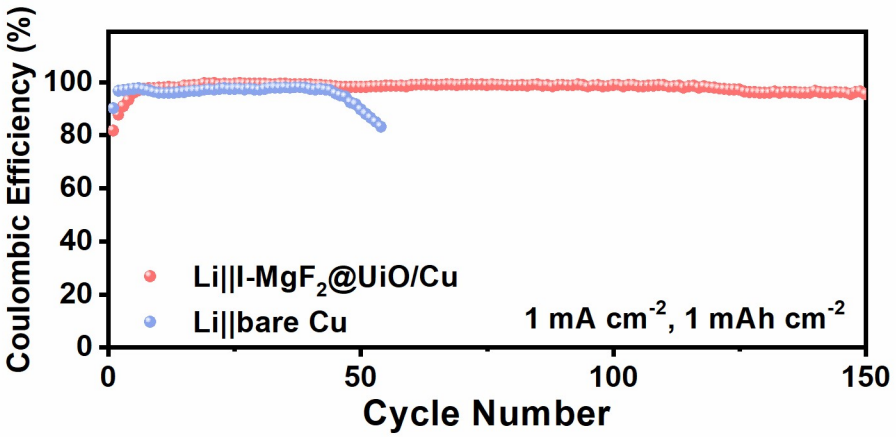

Fig. S27 Comparison of the Coulombic efficiencies of Li||I-MgF_2@UiO/Cu and Li||bare Cu cells at 1 mA cm^{-2} and 1 mAh cm^{-2}.

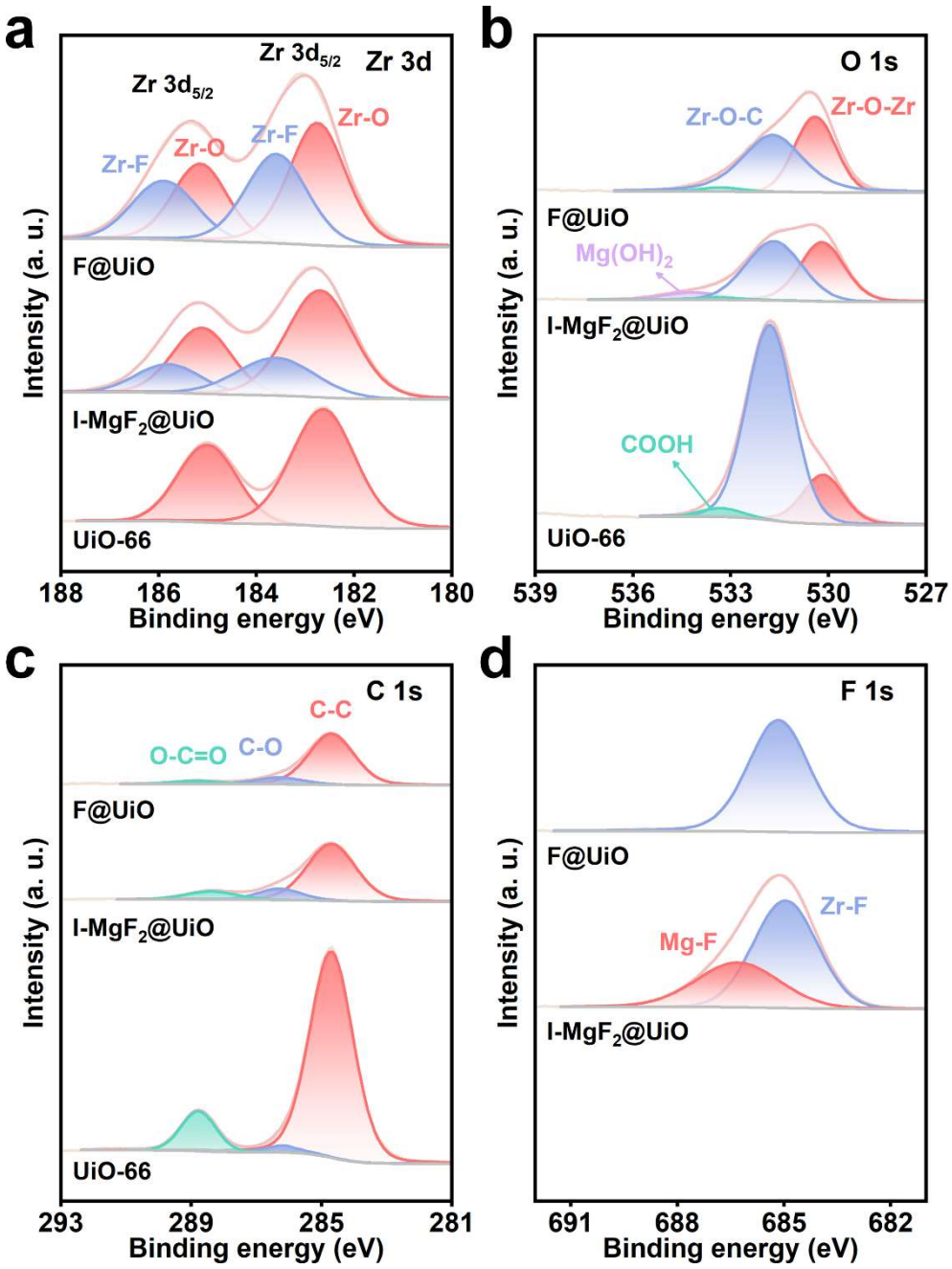

Fig. S28 XPS spectra of F@UiO, I-MgF_2@UiO, and UiO-66 with the signals of a) Zr 3d, b) O 1s, c) C 1s, and d) F 1s.

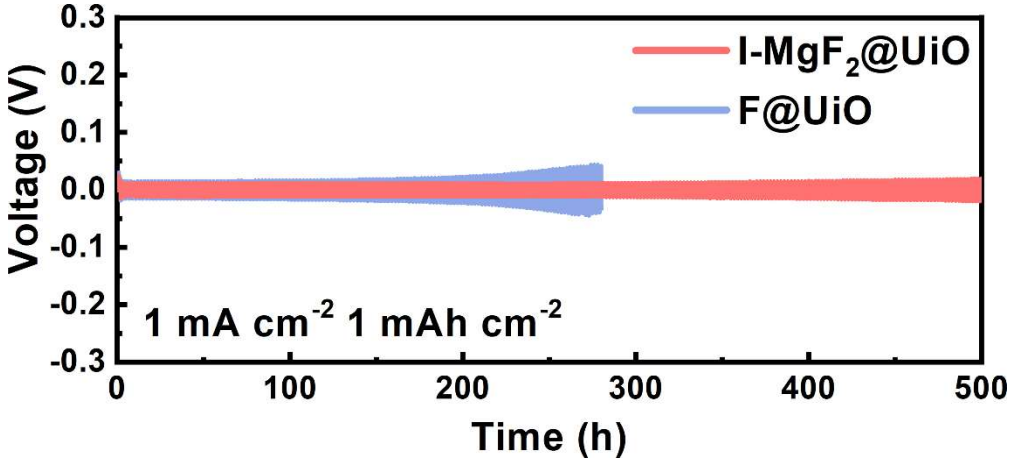

Fig. S29 Voltage profiles of Li||Li symmetric cells with F@UiO and I-MgF_2@UiO at 1 mA cm^{-2} and a capacity of 1 mAh cm^{-2}.

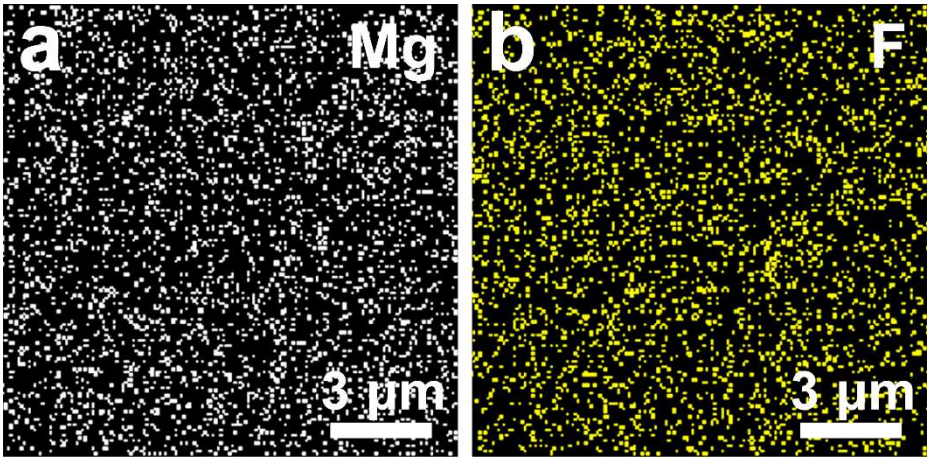

Fig. S30 SEM-EDS elemental mapping images corresponding to Figure 4g.

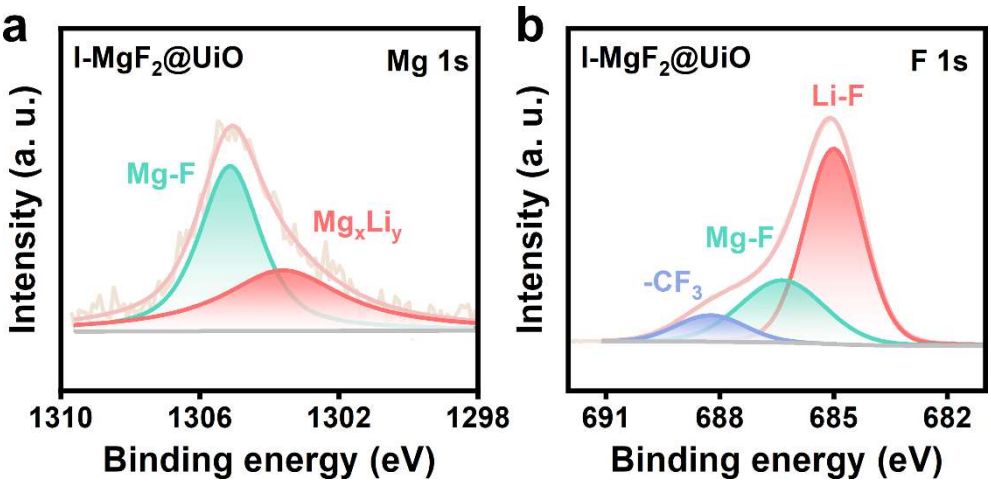

Fig. S31 XPS spectra of a) Mg 1s and b) F 1s in I-MgF_2@UiO electrode after 48 h resting.

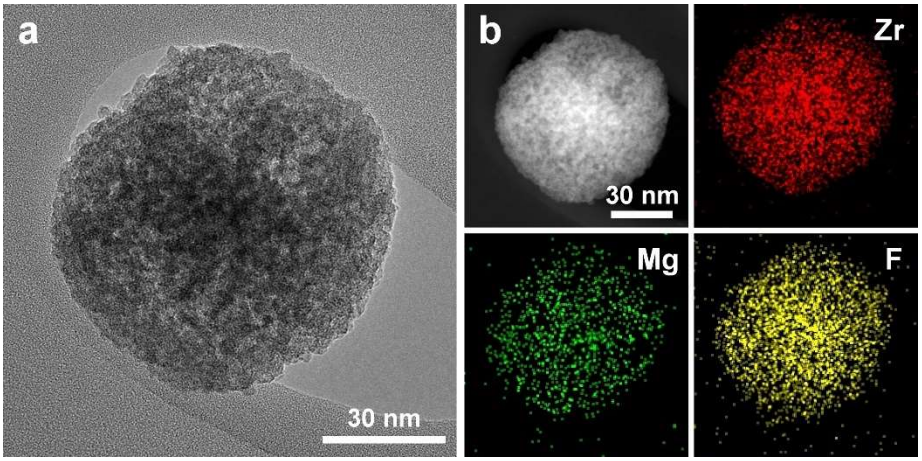

Fig. S32 a) TEM image and b) corresponding EDS mapping images of I-MgF_2@UiO after 10 cycles of Li plating/stripping at 1 mA cm^{-2} and a capacity of 1 mAh cm^{-2}.

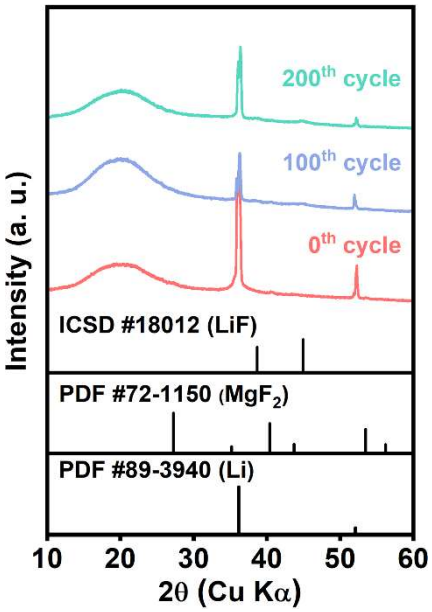

Fig. S33 XRD patterns of I-MgF_2@UiO electrode with coating stripped off before and after the 100th and 200th Li plating/stripping cycles in the 2θ range from 10 to 60°.

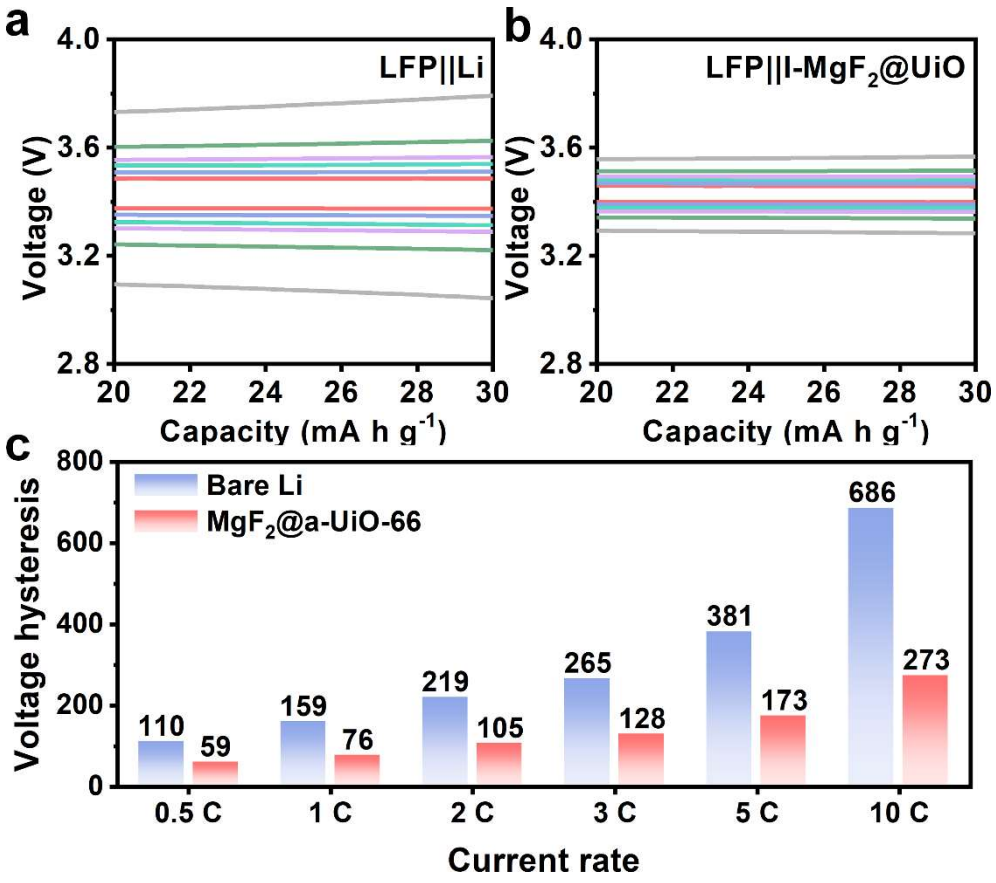

Fig. S34 Galvanostatic charge/discharge profiles of a) LFP||bare Li and b) LFP||I-MgF_2@UiO (magnified figures of Figures 6d and 6e). c) Comparison of voltage hysteresis of LFP||bare Li and b) LFP||I-MgF_2@UiO full cells.

Table S1. ICP-OES result of centrifuged solution after MgF_2 infiltration process to obtain I-MgF_2@UiO.

Element	Concentration
Zr	140.8 ppm

Table S2. Resistances obtained from the fitted Nyquist plots before and after polarization, and currents for t_{Li+} calculation.

Sample	R_{b0} (Ω)	R_0 (Ω)	R_{ss} (Ω)	I_0 (mA)	I_{ss} (mA)	t_{Li+}
Bare Li	17.6	367.2	438.3	0.023	0.014	0.24
UiO-66	19.9	112.3	113	0.076	0.065	0.47
C-MgF_2@UiO	7.0	79.4	85.9	0.103	0.086	0.58
I-MgF_2@UiO	6.2	30.3	31.2	0.185	0.159	0.75

※ Note: R_{b0} represents the bulk resistance before polarization. R_0 and R_{ss} denote the interfacial resistance before and after polarization, respectively. I_0 and I_{ss} are the initial and steady-state currents.

Table S3. Comparison of the lifespan and voltage polarization between Li||Li symmetric cells utilizing I-MgF_2@UiO and previously reported LMA.

Electrode	Electrolyte	Operating condition (mA cm^{-2}/ mAh cm^{-2})	Voltage polarization (mV)	Cycle time (h)	Reference
I-MgF_2@UiO	**1 M LiTFSI**	**0.5/1**	**~7**	**1600**	**This work**
	1 M LiTFSI 2 wt% $LiNO_3$	**1/1**	**~10**	**1500**	**This work**
LiF-rich Li	1 M LiTFSI	1/1	~43	520	[28]
COF-Li	1 M LiTFSI	0.5/1 1/11	~20 ~28	1000 400	[29]
Sb-Li	1 M LiTFSI	0.5/1	~25	1268	[30]
S-COF	1 M LiTFSI 2 wt% $LiNO_3$	1/1	~11	600	[31]
Li/Li-Sn	1 M LiTFSI 2 wt% $LiNO_3$	1/1	~12	900	[32]
Li@G	1 M LiTFSI 2 wt% $LiNO_3$	1/3	~27	400	[33]
Cu@Zn-MOF/PVA	1 M LiTFSI 2 wt% $LiNO_3$	1/1	51.7	580	[34]
Li-rGO	1 M LiTFSI 1 wt% $LiNO_3$	1/1	~14	900	[35]
Ag (Au)-Li	1 M LiTFSI 1 wt% $LiNO_3$	1/1	~25	900	[36]
LSSe@Li	1 M LiTFSI 1 wt% $LiNO_3$	1.5/3 2/1	~17 ~40	900 400	[37]
3D-HCFs@Li	1 M LiTFSI 1 wt% $LiNO_3$	1/1	~18	1200	[38]
CNZ	1 M LiTFSI 1 wt% $LiNO_3$	1/1	~22	1250	[39]
MCF	1 M LiTFSI 1 wt% $LiNO_3$	1/1	~24	400	[40]
CF@PN-CNS-Li	1 M LiTFSI 1 wt% $LiNO_3$	1/1	~12	600	[41]

Table S4. Comparison of overpotentials between I-MgF_2@UiO and bare Li symmetric cells at different current densities.

Sample	Overpotentials (mV)					
	0.5 mA cm^{-2}	**1 mA cm^{-2}**	**2 mA cm^{-2}**	**3 mA cm^{-2}**	**5 mA cm^{-2}**	**10 mA cm^{-2}**
I-MgF_2@UiO	7	11	17	24	35	63
Bare Li	25	45	71	103	-	-

Table S5. Comparison of specific capacities of LFP||I-MgF_2@UiO and LFP||bare Li full cells at various current rates.

Sample	Specific capacity (mA h g^{-1})						
	0.5 C (initial)	**1 C**	**2 C**	**3 C**	**5 C**	**10 C**	**0.5 C**
I-MgF_2@UiO	163.4	159.8	148.5	139.2	124.7	102.1	163.3
Bare Li	138.7	126.8	114.5	104.8	88.7	61.1	135.3

Table S6. Comparison of cycling performance between LFP||Li full cells utilizing I-MgF_2@UiO anode and previously reported LMA.

Electrode	Current rate	Cycle	Discharge capacity (mAh g^{-1})	Reference
I-MgF_2@UiO	**1 C** **10 C**	**300** **2000**	**159.8** **102.1**	**This work**
Li/Li-Sn	0.5 C	300	147.3	[28]
Ag (Au)-Li	0.5 C 1 C	200 100	158.0 147.0	[36]
LSSe@Li	1 C	480	155.0	[37]
3D-HCFs@Li	0.2 C 0.5 C	150 200	154.0 147.0	[38]
CNZ	1 C	300	110.0	[39]
Protected Li	1 C 2 C	500 300	141.0 120.0	[42]
Li@GPCS	0.7 C	600	140.0	[43]
PVdF-HFP-Li	0.5 C	350	153.0	[44]
Zn-MXene-Li	2 C 10 C	170 500	140.0 110.0	[45]
CoP@CNF@Li	5C	1000	115.0	[46]

Supplementary References

1 P. Giannozzi, S. Baroni, N. Bonini, M. Calandra, R. Car, C. Cavazzoni, D. Ceresoli, G. L. Chiarotti, M. Cococcioni and I. Dabo, *J. Phys.-Condes. Matter.*, 2009, **21**, 395502.

2 P. Giannozzi, O. Andreussi, T. Brumme, O. Bunau, M. B. Nardelli, M. Calandra, R. Car, C. Cavazzoni, D. Ceresoli and M. Cococcioni, *J. Phys.-Condes. Matter.*, 2017, **29**, 465901.

3 J. P. Perdew, K. Burke and M. Ernzerhof, *Phys. Rev. Lett.*, 1996, **77**, 3865.

4 S. Grimme, J. Antony, S. Ehrlich and H. Krieg, *J. Chem. Phys.*, 2010, **132**.

5 J. B. Park, C. Choi, S. Yu, K. Y. Chung and D. W. Kim, *Adv. Energy Mater.*, 2021, **11**, 2101544.

6 T. Yan, F. Li, C. Xu and H.-T. Fang, *Electrochim. Acta.*, 2022, **410**, 140004.

7 D. K. Kim, J. B. Park, C. Choi and D.-W. Kim, *Chem. Eng. J.*, 2024, **479**, 147820.

8 L. Yue, X. Wang, L. Chen, D. Shen, Z. Shao, H. Wu, S. Xiao, W. Liang, Y. Yu, and Y. Li, *Energy Environ. Sci.*, 2024, **17**, 1117-1131.

9 T. Naren, G. C. Kuang, R. Jiang, P. Qing, H. Yang, J. Lin, Y. Chen, W. Wei, X. Ji, L. Chen, *Angew. Chem. Int. Ed.*, 2023, **62**, e202305287.

10 J. Yang, F. Zhang, X. Wang, D. He, G. Wu, Q. Yang, X. Hong, Y. Wu and Y. Li, *Angew. Chem. Int. Ed.*, 2016, **55**, 12854-12858.

11 Z. Qin, Z. You, K. N. Bozhilov, S. K. Kolev, W. Yang, Y. Shen, X. Jin, J. P. Gilson, S. Mintova and G. N. Vayssilov, *Chem.-Eur. J.*, 2022, **28**, e202104339.

12 S. Mei, B. Xiang, S. Guo, J. Deng, J. Fu, X. Zhang, Y. Zheng, B. Gao, K. Huo and P. K. Chu, *Adv. Funct. Mater.*, 2023, 2301217.

13 Z. Zhao, M. Qian, J. Wang, W. Cao, X. Qin, P. Guo, S. Hao, R. Wang, F. Wu and G. Tan, *Batteries Supercaps.*, 2022, **5**, e202200232.

14 T. Tanuma, H. Okamoto, K. Ohnishi, S. Morikawa and T. Suzuki, *Appl. Catal. A-Gen.*, 2009, **359**, 158-164.

15 A. Pal, C. Thinaharan, N. G. Krishna, A. R. Shankar and J. Philip, *Appl. Surf. Sci.*, 2022, **578**, 151958.

16 A. Sreedhar, Q. T. H. Ta and J.-S. Noh, *J. Ind. Eng. Chem.*, 2022.

17 Z. Azdad, L. Marot, L. Moser, R. Steiner and E. Meyer, *Sci Rep.*, 2018, **8**, 16251.

18 S. Li, Y. Gan, S. J. Shah, R. Wang, W. Gong, R. Wei, H. Ji, Z. Zhao and Z. Zhao, *Chem. Eng. J.*, 2021, **426**, 131440.

19 L. Wan, G. Ye, Y. Chang, Z. Yang, G. Shi, Q. Zhang and J. Wang, *Microporous Mesoporous Mat.*, 2024, **364**, 112879.

20 C. Jiang, Y. Gu, M. Tang, Y. Chen, Y. Wu, J. Ma, C. Wang and W. Hu, *ACS Appl. Mater. Interfaces*, 2020, **12**, 10461-10470.

21 P. Xiao, X. Yun, Y. Chen, X. Guo, P. Gao, G. Zhou and C. Zheng, *Chem. Soc. Rev.*, 2023.

22 Q. An, H. e. Wang, G. Zhao, S. Wang, L. Xu, H. Wang, Y. Fu and H. Guo, *Energy Environ. Mater.*, 2023, **6**, e12345.

23 Y. Li, W. Chen, T. Lei, H. Xie, A. Hu, F. Wang, J. Huang, X. Wang, Y. Hu and C. Yang, *Energy Storage Mater.*, 2023, **59**, 102765.

24 J. Hu, C. Lai, K. Chen, Q. Wu, Y. Gu, C. Wu and C. Li, *Nat. Commun.*, 2022, **13**, 7914.

25 E. Kemnitz, S. Wuttke and S. M. Coman, *Eur. J. Inorg. Chem.*, 2011, **2011**, 4773-4794.

26 Z. Huesges, C. Müller, B. Paulus, C. Hough, N. Harrison and E. Kemnitz, *Surf. Sci.*, 2013, **609**, 73-77.

27 Z. Liu, W. Chen, F. Zhang, F. Wu, R. Chen, L. Li, *Small*, 2023, **19**, 2206655.

28 Y. Yuan, F. Wu, Y. Bai, Y. Li, G. Chen, Z. Wang and C. Wu, *Energy Storage Mater.*, 2019, **16**, 411-418.

29 D. Chen, S. Huang, L. Zhong, S. Wang, M. Xiao, D. Han and Y. Meng, *Adv. Funct. Mater.*, 2020, **30**, 1907717.

30 T. Chen, W. Kong, P. Zhao, H. Lin, Y. Hu, R. Chen, W. Yan and Z. Jin, *Chem. Mat.*, 2019, **31**, 7565-7573.

31 W. Wang, Z. Yang, Y. Zhang, A. Wang, Y. Zhang, L. Chen, Q. Li and S. Qiao, *Energy Storage Mater.*, 2022, **46**, 374-383.

32 J. Du, W. Wang, M. Wan, X. Wang, G. Li, Y. Tan, C. Li, S. Tu and Y. Sun, *Adv. Energy Mater.*, 2021, **11**, 2102259.

33 B. He, W. Deng, Q. Han, W. Zhu, Z. Hu, W. Fang, X. Zhou and Z. Liu, *J. Mater. Chem. A.*, 2021, **9**, 25558-25566.

34 L. Fan, Z. Guo, Y. Zhang, X. Wu, C. Zhao, X. Sun, G. Yang, Y. Feng and N. Zhang, *J. Mater. Chem. A.*, 2020, **8**, 251-258.

35 D. Lin, Y. Liu, Z. Liang, H.-W. Lee, J. Sun, H. Wang, K. Yan, J. Xie and Y. Cui, *Nat. Nanotechnol.*, 2016, **11**, 626-632.

36 F. Guo, C. Wu, H. Chen, F. Zhong, X. Ai, H. Yang and J. Qian, *Energy Storage Mater.*, 2020, **24**, 635-643.

37 F. Liu, L. Wang, Z. Zhang, P. Shi, Y. Feng, Y. Yao, S. Ye, H. Wang, X. Wu and Y. Yu, *Adv. Funct. Mater.*, 2020, **30**, 2001607.

38 L. Liu, Y.-X. Yin, J.-Y. Li, N.-W. Li, X.-X. Zeng, H. Ye, Y.-G. Guo and L.-J. Wan, *Joule*, 2017, **1**, 563-575.

39 J. Zhang, H. Chen, M. Wen, K. Shen, Q. Chen, G. Hou and Y. Tang, *Adv. Funct. Mater.*, 2022, **32**, 2110110.

40 C. Wei, Y. Wang, Y. Zhang, L. Tan, Y. Qian, Y. Tao, S. Xiong and J. Feng, *Nano Res.*, 2021, **14**, 3576-3584.

41 J. Luan, Q. Zhang, H. Yuan, D. Sun, Z. Peng, Y. Tang, X. Ji and H. Wang, *Adv. Sci.*, 2019, **6**, 1901433.

42 H. J. Liu, C. Y. Yang, M. C. Han, C. Y. Yu, X. Li, Z. Z. Yu and J. Qu, *Angew. Chem. Int. Ed.*, 2023, **135**, e202217458.

43 H. Liu, J. Di, P. Wang, R. Gao, H. Tian, P. Ren, Q. Yuan, W. Huang, R. Liu and Q. Liu, *Carbon Energy*, 2022, **4**, 654-664.

44 B. Xu, H. Zhai, X. Liao, B. Qie, J. Mandal, T. Gong, L. Tan, X. Yang, K. Sun and Q. Cheng, *Energy Storage Mater.*, 2019, **17**, 31-37.

45 J. Gu, Q. Zhu, Y. Shi, H. Chen, D. Zhang, Z. Du and S. Yang, *ACS Nano*, 2020, **14**, 891-898.

46 C. Fu, S. Lin, C. Zhao, J. Wang, L. Wang, J. L. Bao, Y. Wang and T. Liu, *Energy Storage Mater.*, 2022, **45**, 1109-1119.